THE JOURNAL OF PHYSICAL CHEMISTRY C

pubs.acs.org/JPCC Article

Femtosecond Nonlinear Optical Properties of 2D Metallic NbS_2 in the Near Infrared

Melissa Maldonado,[#] Manoel L. da Silva Neto,[#] Pilar G. Vianna, Henrique B. Ribeiro, Vanessa O. Gordo, Isabel C. S. Carvalho, Leonardo de S. Menezes,[*] Cid B. de Araújo, Christiano J. S. de Matos, Leandro Seixas, Ali M. Jawaid, Robert Busch, Allyson J. Ritter, Richard A. Vaia, and Anderson S. L. Gomes

Cite This: *J. Phys. Chem. C* 2020, 124, 15425−15433 Read Online

ACCESS | Metrics & More | Article Recommendations | Supporting Information

ABSTRACT: The understanding of the nonlinear optical (NLO) properties of photonic materials is relevant and necessary for basic studies and technological developments. Among the materials with high optical nonlinearities, layered transition-metal dichalcogenides (LTMDs) have attracted considerable attention from the viewpoint of both synthesis as well as characterization and applications. We report here the third-order NLO properties of one LTMD—the metallic NbS_2—that was prepared by a modified redox exfoliated method, suspended in acetonitrile. The LTMD was morphologically and compositionally characterized using transmission electron microscopy, atomic force microscopy, X-ray diffraction, Raman scattering, and linear absorption. The Z-scan technique was employed to characterize the nonlinear refraction (NLR) and nonlinear absorption (NLA) behavior in the femtosecond regime. Metallic NbS_2 presented a sign inversion of the nonlinear refractive index from negative (self-defocusing) to positive (self-focusing) with the increase of intensity up to 100 GW/cm^2. Two distinct features characteristic of NLA, two-photon absorption and saturated absorption, were also observed for different intensity ranges, with the former evolving into the latter as the intensity increased in the same range as for the NLR measurements. The material's band structure of NbS_2 was calculated using the density functional theory, and the origin of the nonlinearities is discussed by comparison with the experimental data.

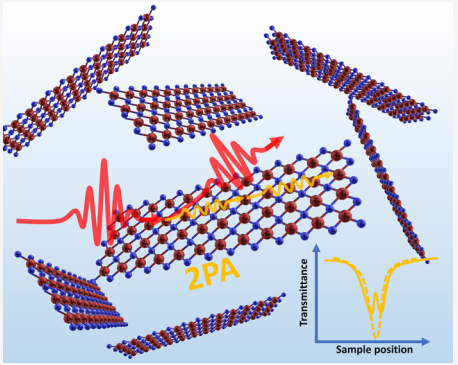

1. INTRODUCTION

The unique properties of nanoscale layered materials have paved the way to a myriad of opportunities for preparation, characterization, and applications of advanced and functional nanomaterials, as recently reviewed in.[1−4] Among the applications, optoelectronics,[5] biomedics,[6] and nonlinear optics[7] have received considerable attention. Nonlinear optical (NLO) effects including second-,[8,9] third-[10,11] and fourth-[12] harmonic generation, as well as sum-frequency generation[13] and high-order harmonic generation,[14] have been demonstrated. Other third-order NLO processes also reported were four-wave mixing,[14] saturated absorption,[15,16] two-photon absorption (TPA),[16−18] and optical limiting.[19,20] The materials can be studied as individual flakes, thin films, or in liquid suspensions.

Nonlinear refraction (NLR) and nonlinear absorption (NLA), which are directly related to the real and imaginary parts of the third-order optical susceptibility, respectively, were studied in MoX_2 (X = S, Se and Te),[21] WS_2,[22] and WS_2, WSe_2, MoS_2, and $Mo_{0.5}W_{0.5}S_2$[23] in different spectro-temporal regimes including visible-NIR wavelengths (532 nm-1064 nm) with ps/fs pulses. In ref 21, the authors characterized MoS_2, $MoSe_2$, and $MoTe_2$ dispersed in cyclohexyl pyrrolidinone (CHP) after liquid exfoliation (LPE). They estimated ∼8 nm thick nanosheets in MoS_2, corresponding to ∼15 monolayers. Among the NLO characterization studies, they measured NLA with Z-scan using 100 fs pulses at 1 kHz and 800 nm. They observed saturable absorption (SA) for all three samples and attributed it to the predominance of multilayer nanosheets in the MoX_2 dispersions, whose band gap energy is smaller (∼1.2 eV) than the photon energy (1.55 eV). Zheng et al., in ref 22, reported on NLO characterization of a WS_2 monolayer grown on 1 mm thick sapphire substrates by chemical vapor deposition. The authors employed the same spectro-temporal regime discussed here (100 fs, 1 kHz, 800 nm with maximum energy of 0.8 mJ). Using the Z-scan technique, they analyzed

Received: March 17, 2020
Revised: June 14, 2020
Published: June 30, 2020

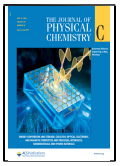

https://dx.doi.org/10.1021/acs.jpcc.0c02383
J. Phys. Chem. C 2020, 124, 15425−15433

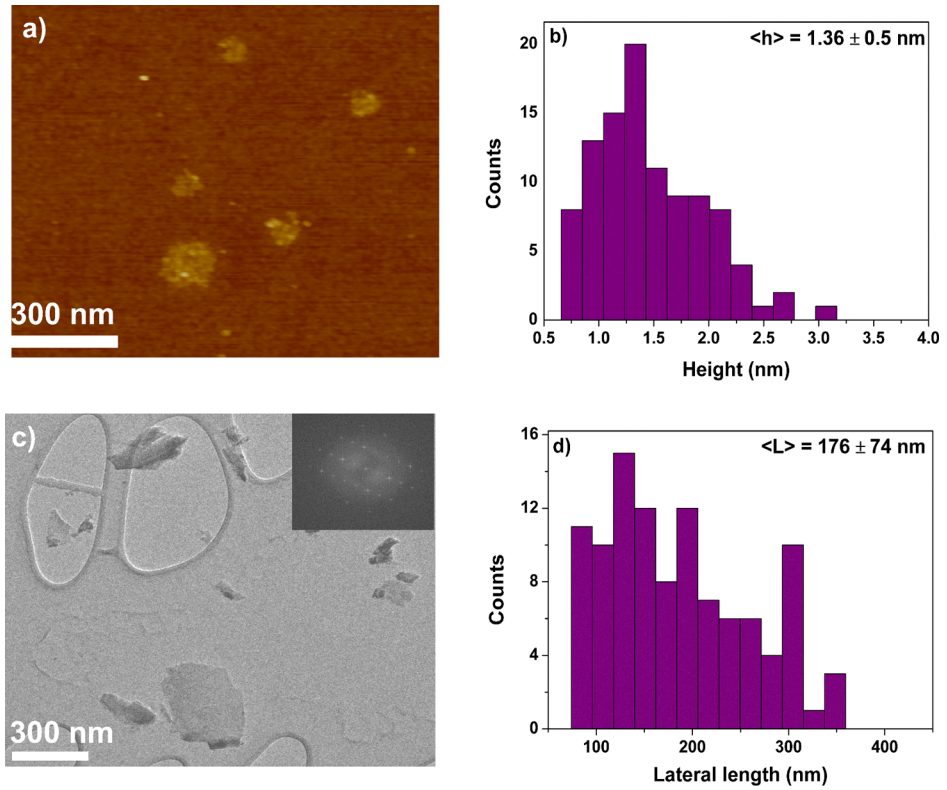

Figure 1. Morphology of exfoliated NbS_2 flakes. AFM (a) provided height distribution (b), and TEM (c) provided lateral size distribution (d) of NbS_2 flakes. Note that the average height reported via AFM analysis is typically larger than the absolute particle size because of substrate−flake interactions.

both the NRL and NLA. In the NLR measurements, an extremely high nonlinear refractive index of $(8.1 \pm 0.4) \times 10^{-9}$ cm^2/W was reported. Bearing in mind that the energy gap of monolayer WS_2 was 2 eV, ref 22 and refs therein, and the excitation energy was 1.55 eV, one-photon excitation cannot occur, and therefore SA would not be expected, contrary to the experimental observation in ref 22 for intensities up to 275 GW/cm^2. For excitations well beyond this value, namely higher than 850 GW/cm^2 up to 2011 GW/cm^2, the SA reversed to a TPA-like open-aperture Z-scan curve (minimum at the focal point). To explain the data, the authors of ref 22 considered an intensity-dependent absorption $\alpha\ (I) = \alpha_0 + \alpha_{NL}I$, and the calculations led to $\alpha_{NL} = -(3.7 \pm 0.28) \times 10^5$ cm/GW.

Among the diversity of methods to fabricate layered transition-metal dichalcogenides (LTMDs),[1−4] redox exfoliation, ref 24 and refs therein, offers features that are critical to composite, coating, and ink technologies, including low cost and low energy. The method, whose result is a stable suspension of submicron platelets of few-layer material, is applicable to exfoliating a wide range of LTMDs from Groups IV, V, VI, and VII allowing preparation of 2D suspensions of less-conventional and, thus, less-studied LTMDs.

In this work, we report on the third-order NLO properties of a less-studied 2D LTMD in suspension and the metallic NbS_2 in the 2H phase, prepared by a modified redox exfoliation method.[24] The optical studies were carried out at 800 nm (1 kHz, 100 fs) using the Z-scan method[25,26] with the LTMD suspended in acetonitrile (ACN). The NLO characteristics of the metallic NbS_2 are compared with those of more conventional LTMDs, including MoS_2, as similar data for the femtosecond NLO response of NbS_2 have not been found in the literature. The origin of the optical nonlinearities is discussed with basis on the calculated band structure of the material and the excitation photon energy employed.

2. METHODS

2.1. Synthesis and Morphological Characterization.

2.1.1. Materials. NbS_2 was purchased from Johnson and Mathley Electronics; MoS_2 was purchased from Sigma Aldrich; Acetonitrile was purchased from VWR and distilled under nitrogen and stored under activated molecular sieves to prevent moisture accumulation. Cumene hydroperoxide (technical grade, 80%) and hydroquinone (reagent grade, 99%) were purchased from Sigma-Aldrich.

2.1.2. Exfoliation of MoS_2. The exfoliation of MoS_2 was performed via the redox exfoliation method.[24] For completeness, the process is described in full. Acetonitrile (50 mL) and cumene hydroperoxide (1 mmol) were added to a round bottom flask and stirred until thoroughly mixed. Afterward, 1600 mg of MoS_2 (10 mmol) was added in one portion, and the slurry was allowed to stir for 24 h at 35 °C under an argon atmosphere. Subsequently, a solution of hydroquinone (2 mL, 0.2 M) was added in one portion and stirred for 45 min. The redox treatment results in in-situ formed polyoxometalates that facilitate surface adsorption and exfoliation via Columbic repulsion.[24] To accelerate this process, a high-speed homogenizer (Turrax T18) was attached, and the solution was mixed for 8 h, resulting in colloidally stable platelets in acetonitrile. After exfoliation, the slurry is washed three times via centrifugation (9 k rpm; 45 min), removal of solvent, and redispersion in fresh anhydrous acetonitrile (this process removes excess oxidants and reductants from the solution).

https://dx.doi.org/10.1021/acs.jpcc.0c02383
J. Phys. Chem. C 2020, 124, 15425−15433

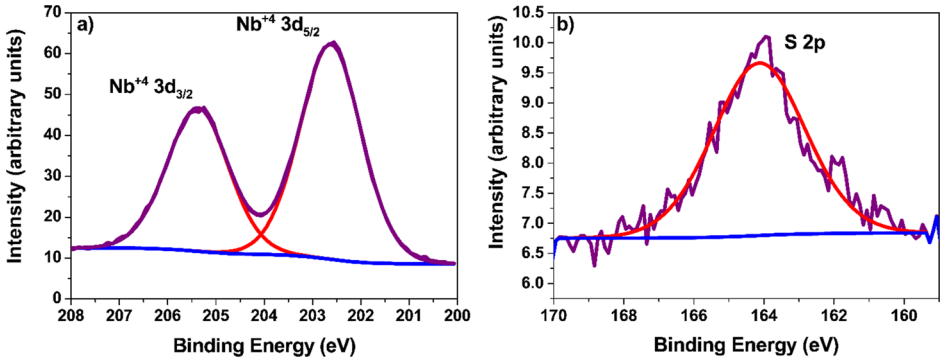

Figure 2. Compositional analysis of NbS_2. XPS spectroscopy of Nb 3d (a) and S 2p (b) regions indicates the presence of both compositional NbS_2. Raw data are shown as purple curves, base line as blue, and spectral envelope fits in red.

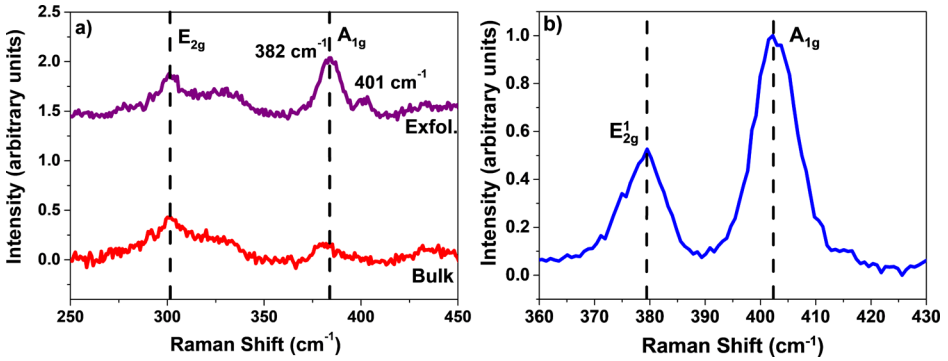

Figure 3. Raman spectra of drop-cast redox exfoliated (a) NbS_2 and (b) MoS_2. Raman spectroscopy of NbS_2 flakes resolves the E_{2g} and A_{1g} vibrational modes. For comparison, a bulk NbS_2 powder was also measured to ensure consistency of material composition.

After three cycles of washing, the slurry containing bulk and exfoliated MoS_2 is referred to as a cleaned LTMD slurry.

2.1.3. Exfoliation of NbS_2. Exfoliation and monolayer selection of NbS_2 were carried out as outlined in the MoS_2 section. All samples for X-ray photoelectron spectroscopy (XPS), Raman, and atomic force microscopy (AFM) were prepared in inert atmospheres with little exposure to ambient conditions to minimize surface oxidation. We note that in the solid-state phase, NbS_2 is known to oxidize quickly[27] when exposed to ambient moisture. Thus, all samples were prepared and stored in anhydrous ACN to minimize surface oxidation of NbS_2.

2.1.4. Monolayer Size Selection of MTSDs. Monolayer selection was carried out via previously described methods.[28] The cleaned LTMD slurry containing bulk and exfoliated LTMDs was centrifuged at 400 rpm for 3 h. The supernatant containing exfoliated NbS_2 was collected and subjected to another round of centrifugation at 500 rpm for 3 h, resulting in sedimentation of large, unexfoliated crystallites. The supernatant was collected and subsequently centrifuged at 700 rpm for 3 h. The light olive (NbS_2) and greenish-yellow (MoS_2) colored solutions were extracted, and AFM measurements were performed to verify monolayer selection.

2.1.5. AFM Measurements. LTMD flakes were measured in noncontact tapping mode on Dimension Icon (Bruker Corporation) with a 10 nm tip diameter Al reflex-coated cantilever (10 N/m). Samples were prepared by drop-casting a dilute solution ($\sim 10^{-9}$ M) of LTMD on an UVO-treated Si substrate. Samples were allowed to dry under dry N_2 at 100 °C (1 h) to ensure complete removal of solvent. Samples were analyzed immediately after exposure to ambient to minimize the influence of surface oxidation.

2.1.6. Electron Microscopy. High-resolution transmission electron microscopy (HRTEM) images were collected using an aberration-corrected FEI Talos transmission electron microscope with an accelerating voltage of 200 kV. Samples were drop-cast (10^{-9} M) onto TEM grids and allowed to dry under dry N_2. After drying, the samples were immediately transferred to the load-lock chamber for imaging. Figure 1 shows the AFM and HRTEM images for the NbS_2 samples.

2.1.7. X-ray Photoelectron Spectroscopy. The XPS analysis was carried out using an SSI XPS System. Survey spectra were acquired using a monochromated Al K_α X-ray source (1486.6 eV) operated at 120 W (10 mA, 10 kV) with the electron analyzer operating in hybrid lens mode and an aperture size of approximately 800 μm^2. Samples were drop-cast on Si wafers (10^{-3} M) and allowed to dry under dry N_2 at 100 °C (1 h) to ensure complete removal of solvent. After drying, samples were immediately transferred to the load-lock chamber to minimize surface oxidation.

Figure 2 shows the results obtained from the compositional characterizations. The Nb region indicates that no surface oxides (Nb $3d_{5/2}$ 206 eV) are present (Figure 2a). Similarly, the S 2p indicates that SO_x species are not present on the surface (S 2p SO_x = 168 eV). For the S 2p region, the small splitting of S 2p (0.92 eV) prevents resolution of the S 2p 1/2 and S 2p 3/2 peaks. Thus, a single gaussian was used to fit the region (Figure 2b).

2.1.8. Raman Spectroscopy. The Raman spectroscopy characterization was carried out in dried individual redox exfoliated flakes on a SiO_2/Si substrate. Raman spectra were

https://dx.doi.org/10.1021/acs.jpcc.0c02383
J. Phys. Chem. C 2020, 124, 15425−15433

collected with a Renishaw inVia Raman microscope and with a WITec Alpha 300R microscope. Prior to material deposition, the substrates (SiO_2/Si) were cleaned with acetone, dried under a nitrogen stream, and immediately treated in an ozone chamber for 15 min to remove surface organic contaminants. This treatment creates a hydrophilic surface that allows for uniform deposition of NbS_2 solutions in acetonitrile.

NbS_2 was drop-cast from a solution of ACN (5 μL; 10 mg/mL NbS_2) onto the cleaned wafers and allowed to dry naturally. The solution wets the substrate completely, and all solvent evaporates within 5 s. The samples were then immediately analyzed via Raman spectroscopy, as surface oxidation of thin NbS_2 occurs rapidly.[29] The excitation laser (514.5 nm) was focused on to the few-to-monolayer flakes with a 20× objective lens. The power was maintained to 100 μW in order to minimize sample heating. Spectra were collected at acquisition times between 60 and 180 s.

Figure 3a shows the obtained Raman spectra. The spectrum of exfoliated NbS_2 flakes is compared with an unexfoliated (bulk) powder, revealing noticeable differences. The peaks identified at 382 and 401 cm^{-1} correspond to the A_{1g} vibrational mode while the peak at 300 cm^{-1} corresponds to the E_{2g} vibrational mode, consistent with literature reports indicating one to three layers of NbS_2.[29] As a further comparison, Figure 3b shows the Raman spectrum of a dried MoS_2 redox exfoliated flake prepared in a similar way (532 nm excitation and a 100× objective lens, to ensure that a single flake was probed, were used in this case). The ∼23 cm^{-1} peak separation reveals a few-layer thickness, further confirming the effectiveness of the exfoliation and size selection procedure.

2.1.9. UV−Vis−NIR Spectroscopy. UV−Vis spectra of exfoliated samples were measured on a Cary 5000 Spectrophotometer. Absorbance and extinction measurements of the samples were performed using the diffuse reflectance accessory for Cary 5000. The corresponding results are seen in Figure 4. The metallic character of NbS_2 is clearly reflected in its absorption spectrum, which does not present any distinct feature in the visible and near-infrared ranges.[24,30,31]

2.2. NLO Characterization. The NLO characterization was performed using the well-established Z-scan method,[25,26] and Figure 5 shows the experimental scheme used.

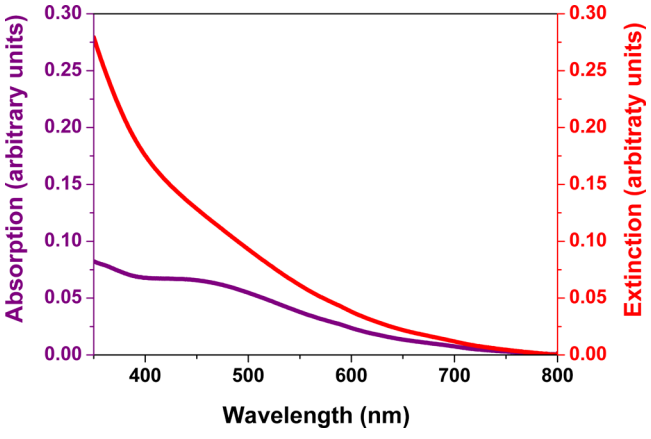

Figure 4. UV−vis spectroscopy was performed on NbS_2 dispersions in ACN (10 mg/mL). The absorption (purple line, left axis) and extinction (red line, right axis) values were measured, and because of the metallic nature of NbS_2, the absorption curves are fairly featureless.

Simultaneous measurements of the NLR and NLA were made, which were normalized to the shot-to-shot fluctuations of the excitation source. The light source was a Ti:Sapphire-based regenerative amplifier (800 nm) operating at 1 kHz and delivering 100 fs single pulses with a maximum energy of 1 mJ. The beam was focused with 15 cm focal length lens onto a 1 mm quartz cuvette. The peak intensity was varied up to I = 140 GW/cm^2 (corresponding to a maximum fluence F = 75.6 mJ/cm^2) for the present experiment.

3. RESULTS

3.1. NLR Measurements. As control experiments, the NL refractive index, n_2, and NLA coefficient, $\alpha_2(I)$, were initially characterized for the solvent (pure ACN) and for MoS_2 flakes prepared by the same method and suspended in ACN. Pure ACN showed a positive (self-focusing) NLR with the value of $n_2(\mathrm{ACN}) = 1.9 \times 10^{-17}$ cm^2/W, compatible with the literature,[32] as shown in Figure 6a,b. The $n_2 \times I$ curve, as shown in Figure 6b, was a constant, indicating that third-order NLR was the dominant mechanism at such excitation conditions for pure ACN. Figure 6c shows the NLR data of MoS_2 at 35 GW/cm^2, which has the same positive sign as for pure ACN in the same intensity range. The measured value of the NLR was $n_2(MoS_2) = +(4.5 \pm 0.3) \times 10^{-16}$ cm^2/W, which is 1 order of magnitude larger than pure ACN. The poor fitting, as shown in Figure 6c, is due to the fact that we did not consider higher order effects. For MoS_2, in the intensity range mentioned, fifth-order effects take place, but we defer this analysis for MoS_2 for a separate publication because this effect was not observed in NbS_2, whose analysis is the object of the present research.

Open-aperture measurements for both the pure ACN and MoS_2 did not show any results for the range of intensities employed, and therefore, NLA was negligible.

In contrast, the exfoliated metallic NbS_2 showed a quite interesting behavior for the NLR, as shown in Figure 7. An inversion in the sign of the NLR as the intensity increased was observed, changing from negative (self-defocusing) for intensities below ∼22 GW/cm^2 (F = 34.9 mJ/cm^2) to positive (self-focusing) above this critical intensity. This is clearly seen in the Z-scan profiles, as shown in Figure 7a,b, and in the $n_2 \times I$ plot, as shown in Figure 7c. The calculated value of n_2 for intensities above the critical value of ∼22 GW/cm^2 (F = 8 mJ/cm^2) is $(3.0 \pm 0.2) \times 10^{-16}$ cm^2/W, as shown in Table 1.

3.2. NLA Measurements. The open-aperture Z-scan allows the measurement of the NLA coefficient, which was observed in the NbS_2 sample, as shown in Figure 8. The NLA profile varies as a function of intensity, changing from a TPA to two-photon saturated absorption (TPSA) at the approximate intensity of I = 65.2 GW/cm^2 (F = 41 mJ/cm^2). This behavior is probably associated to the change in NLR because after saturation is reached, the nonlinear refractive index changes accordingly via a nonlinear Kramers−Kronig relation. The solid curves on the data were obtained as described in a section below.

3.3. Atomistic Simulations. Before discussing the above results, we describe here the first-principles calculations method, based on the density functional theory (DFT),[33,34] as implemented in SIESTA code[35] to calculate the electronic properties of NbS_2. We used localized double-ζ basis (DZP), with an energy shift of 0.03 eV and a mesh cutoff of 400 Ry. We also used norm-conserved pseudopotentials with Troullier-Martins parameterization.[36] For the exchange−correlation

https://dx.doi.org/10.1021/acs.jpcc.0c02383
J. Phys. Chem. C 2020, 124, 15425−15433

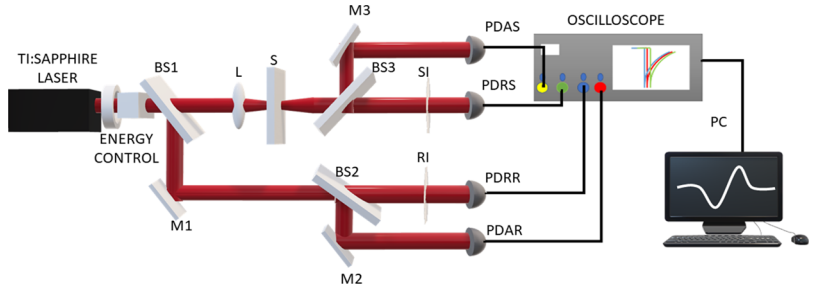

Figure 5. Z-scan technique setup for simultaneous closed- and open-aperture measurements. The laser beam passed through a half-wave plate and a polarizer for the pulse energy control. BS1, BS2, and BS3 are beam splitters; M1, M2, and M3 are mirrors; L is the focusing lens; S is the sample; SI and RI are the closed-aperture signal and reference irises, respectively; PDAS (PDRS) is the signal photodetector for the NLA (NLR) channel while PDAR (PDRR) is its reference photodetector.

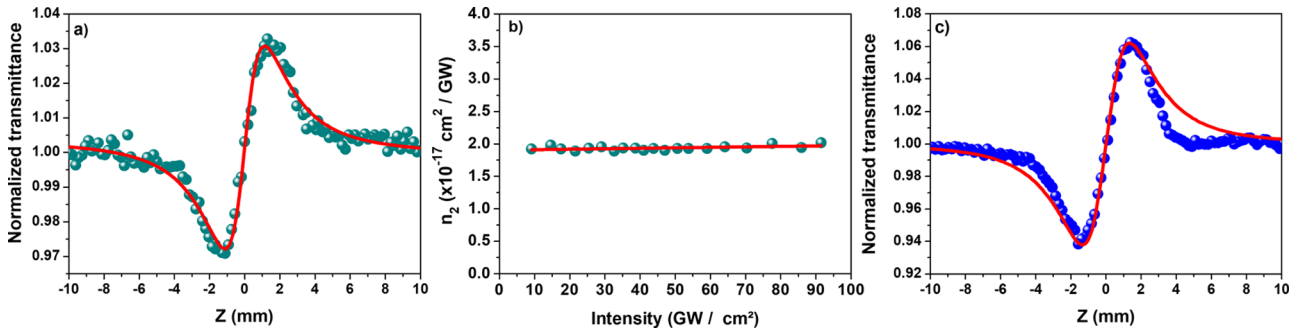

Figure 6. Closed-aperture Z-scan curve for ACN at I = 70 GW/cm^2 (F = 44 mJ/cm^2); (b) intensity dependence of n_2; and (c) closed-aperture Z-scan curve for MoS_2 at I = 35 GW/cm^2 (F = 22 mJ/cm^2). The continuous lines in (a,c) are theoretical fits (see eq 1 and text for the fitting results).

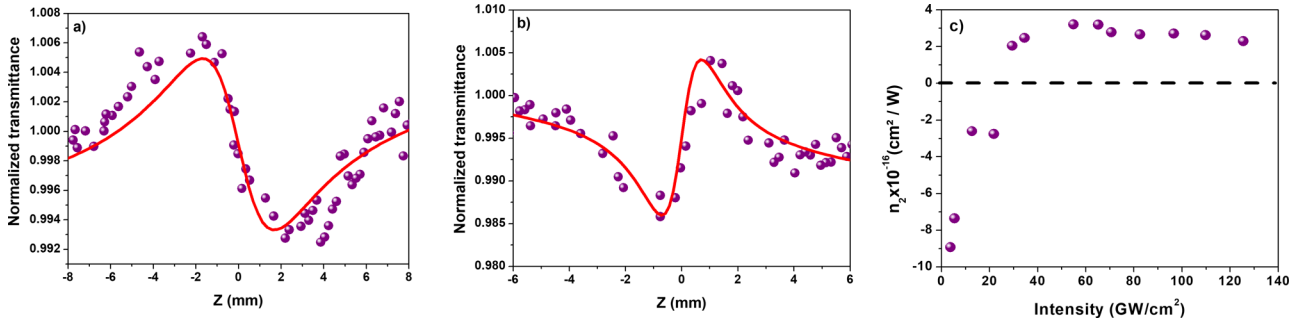

Figure 7. Closed-aperture measurements for NbS_2 (a) below the critical intensity of ∼22 GW/cm^2 (F = 34.9 mJ/cm^2), (b) above the critical intensity, and (c) effective $n_2 \times I$ plot, showing the critical intensity whereby the sign of the NLR changes, $I_C \sim 25$ GW/cm^2.

Table 1. Experimentally Determined Values of the NLR and NLA Coefficients for the NbS_2 Suspension and Related Literature Values for Other LTMDs in the Same Spectro-Temporal Regime (800 nm, ∼100 fs)[a]

sample	solvent/substrate	$n_2 \times 10^{-16}$ (cm^2/W)	α_2, η_2 (cm/GW)	I_S (GW/cm^2)	refs
NbS_2	ACN	+(3.0 ± 0.2) ($I > I_c$)	$\alpha_2 = 2.1 \times 10^{-1}$, $\eta_2 = -1.1 \times 10^{-1}$	52	this work
MoS_2	ACN	+(4.5 ± 0.3)			this work
MoS_2	NMP	NA	$\alpha_2 = 4.6 \times 10^{-3}$	413 ± 24	15
MoS_2	CHP	NA	$\alpha_2 = -2.4 \times 10^{-2}$	381 ± 346	21
Graphene	CHP	NA	$\alpha_2 = -1.5 \times 10^{-2}$	538 ± 127	21
WS_2	sapphire	+1.2	$\alpha_2 = -3.7 \times 10^{-5}$	NA	22

[a]ACN—acetonitrile; NMP—*N*-methylpyrrolidone; CHP—cyclohexylpyrrolidinone.

functional, we use the Vydrov-van Voorhis functional (VV10),[37] which includes nonlocal terms for the correction of van der Waals forces. The Brillouin zone sampling was based on the Monkhorst−Pack method,[38] with 20 × 20 × 1 grid for monolayers and 20 × 20 × 7 grid for bulks. For density of states calculations, we use thinner grids of 200 × 200 × 1 for the monolayer and 80 × 80 × 40 for bulk. All geometries were completely relaxed until forces less than 0.001 eV/Å.

4. DISCUSSION

To determine the NLO coefficients, we employed the known equations for the closed- and open-aperture Z-scan.[25,26] The expression in eq 1 was used for the closed-aperture Z-scan

https://dx.doi.org/10.1021/acs.jpcc.0c02383
J. Phys. Chem. C 2020, 124, 15425−15433

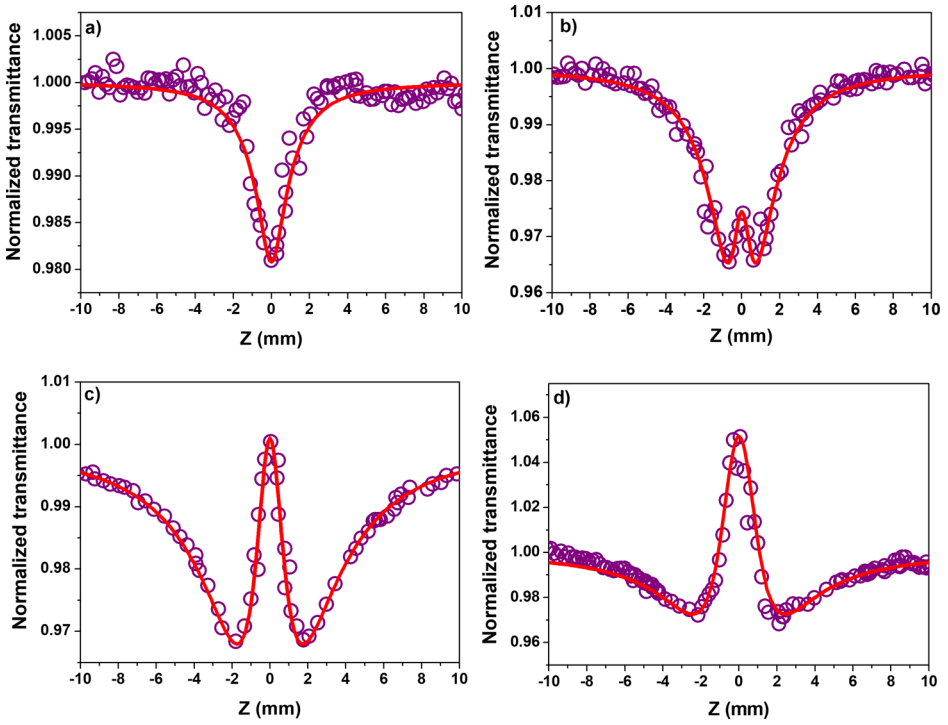

Figure 8. NLA measurements for sample NbS_2 for (a) I = 12.7 GW/cm^2 (F = 8 mJ/cm^2), (b) I = 65.2 GW/cm^2 (F = 41 mJ/cm^2), (c) I = 96.5 GW/cm^2 (F = 60.7 mJ/cm^2), and (d) 125.6 GW/cm^2 (F = 79.1 mJ/cm^2).

$$T = 1 + \frac{4\Delta\Phi^{(3)}a}{(a^2+1)(a^2+9)} \quad (1)$$

where $\Delta\Phi^{(3)} = kn_2I\left(\frac{1-\exp(-\alpha_0 L)}{\alpha_0}\right)$, k is the wavevector, n_2 is the third-order nonlinear refractive index, α_0 is the linear absorption coefficient, L is the sample length, and $a = z/z_0$, where z is the sample position and z_0 is the Rayleigh parameter.

The open-aperture Z-scan scheme gives information on the NLA, which can be because of TPA or multiphoton absorption (MPA), saturated absorption (SA), reverse saturation absorption, or TPSA. These phenomena have been identified in MoS_2 and WS_2[19−23] at intensities higher than 200 GW/cm^2 and using appropriate excitation photon energies compared to the band gap of the material studied. The equations used to fit the experimental data depend upon the model employed, which can include nonsaturable or saturable TPA because of hyperbolic homogeneously or inhomogeneously broadening models, ref 16 and refs therein. To fit our experimental results in NbS_2, we investigated contributions for the open-aperture Z-scan profile because of saturation of the linear absorption coefficient, TPA saturation, and nonlinear light scattering (NLS), as illustrated in the Supporting Information. The best fitting corresponding to the solid curves of Figure 8 was obtained considering saturation of TPA and contribution of NLS, which is relevant for intensities larger than 60 GW/cm^2, according to eq 2

$$\alpha(I) = \alpha_0 + \frac{\alpha_2 I}{\sqrt{1 + I^2/{I_S}^2}} + \eta_2 I \quad (2)$$

where α_0 is the linear absorption coefficient, α_2 is the TPA coefficient, I_S is the TPA saturation intensity, and η_2 is the nonlinear scattering coefficient.

The solid lines, as shown in Figure 8, were fitted considering the effect of inhomogeneous broadening. Other mechanisms were evaluated as discussed in the Supporting Information but they could not reproduce the Z-scan profiles. The saturation intensities obtained, as well as the coefficients α_2 and η_2, are shown in Table 1 (with α_0 = 8.2 cm^{-1} at 800 nm), together with literature values for other LTMDs. Also, Table 1 shows the value of n_2 for MoS_2 in ACN, which is of the same order as for NbS_2 (for intensities above I_S) but does not present inversion of sign in the whole range of intensities used.

Although we compared our data from the metallic NbS_2 with semiconducting TMDs, for the lack of literature data or the metallic material, as highlighted in the introduction, it is worth mentioning, without any direct comparison, that two-photon processes have been studied in gold nanoparticles and clusters, as reviewed by Olesiak-Banska et al.[39] In their review, qualitatively similar behavior was reported with open-aperture Z-scan measurements for gold as for NbS_2, although the closed-aperture measurements did not report the sign inversion observed in our case. Values of the nonlinearity are a few orders of magnitude higher than reported here, which are dependent on excitation close to gold plasmonic resonance, as well as the shape of the nanomaterials (nanoparticles, nanorods, nanoshells, and nanoclusters). Further details are seen in ref 39.

We also investigated the nonlinear light scattering (NLS) properties of the NbS_2 suspension by measuring the scattered intensity as a function of input intensity, as in ref 19, and the results are shown in Figure 9. Notice that the scattered intensity starts to deviate from a linear response at around 75 GW/cm^2. We recall that NLS[40] can play a role in the optical nonlinearity of nanoscatters, leading to, for example, an optical limiting behavior in LTMDs.[19]

To understand qualitatively the origin of the nonlinearity in NbS_2, we calculated the electronic band structure of 2H−NbS_2

https://dx.doi.org/10.1021/acs.jpcc.0c02383
J. Phys. Chem. C 2020, 124, 15425−15433

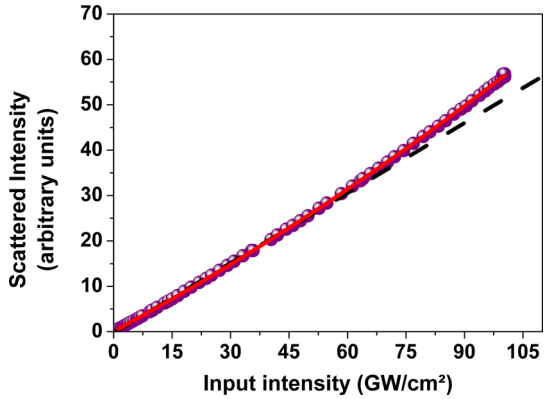

Figure 9. Scattered light intensity behavior versus the input laser intensity in the NbS_2 suspension.

monolayer and bulk with first-principles methods based on DFT as described before, whose results are shown in Figure 10. For the monolayer, we indicate possible electronic transitions for one-photon and TPA for incident laser photons with an energy of 1.55 eV (~800 nm). In principle, to conserve angular momentum, one-photon transitions must occur from bands with major S compositions (p orbitals) to bands with primary Nb composition (d orbitals) while two-photon transitions may occur between two bands with major Nb composition or from a band with major S composition to a band with mixed composition. If the material is doped with electrons, it can also make electronic transitions for TPA in a van Hove singularity at the *K* point. For this van Hove singularity, there is a peak in the density of states that can increase the optical absorption. Similar results for the monolayer band structure are shown in ref 41.

A qualitative analysis of Figure 10 shows that both one-photon absorption and TPA are allowed. In particular, for doped NbS_2, the two-photon process may involve a van Hove singularity, which would greatly enhance the NLA. Indeed, doping might also explain, via Pauli blocking, the negligible absorption at 800 nm (1.55 eV), as shown in Figure 4. Further increase in input pump intensity leads to TPA saturation, as observed in our experiments. The negative n_2 sign for intensities below the critical intensity to induce the NLR sign change is consistent with this behavior. As we mentioned before, the change in sign of n_2 may follow from the change in sign in the NLA because n_2 and α_2 are related via the nonlinear Kramers–Kronig relation. However, a quantitative description of the entire phenomena is beyond the scope of this work.

5. CONCLUSIONS

In summary, we studied the NLO behavior of metallic NbS_2 prepared by a modified redox exfoliation technique. NLR because of the third-order susceptibility was characterized, and a nonlinear refractive index $n_2 = (3.0 \pm 0.1) \times 10^{-16}$ cm^2/W was measured, with a change in nonlinear refractive index from negative to positive as a function of the laser intensity. NLA was measured and quantified as $\alpha_2 = 2.1 \times 10^{-1}$ cm/GW, showing saturation of TPA at a saturation intensity $I_S = 52$ GW/cm^2. Nonlinear light scattering was also observed for large incident laser intensity. The present results suggest interesting applications of NbS_2. For instance, ultrashort pulse generation in a fiber laser using NbS_2 as a saturable absorber has been demonstrated.[42] As a novel application, NbS_2 can be exploited for nonlinear light propagation effects related to spatial solitons, as reported for other nanostructured systems.[43] Further work will expand the wavelength range of NLO characterization for this material, particularly to the blue spectral region.

■ ASSOCIATED CONTENT

Supporting Information

The Supporting Information is available free of charge at https://pubs.acs.org/doi/10.1021/acs.jpcc.0c02383.

Theoretical studies are presented taking into account diverse relative contributions from different nonlinear optical absorption (NLA) processes as well as three different NLA broadening models in order to try to fit the saturation behavior of TPA (PDF)

■ AUTHOR INFORMATION

Corresponding Author

Leonardo de S. Menezes − *Physics Department, Universidade Federal de Pernambuco, 50670-901 Recife-PE, Brazil;* orcid.org/0000-0002-8654-1953; Email: lmenezes@df.ufpe.br

Authors

Melissa Maldonado − *Physics Department, Universidade Federal de Pernambuco, 50670-901 Recife-PE, Brazil*

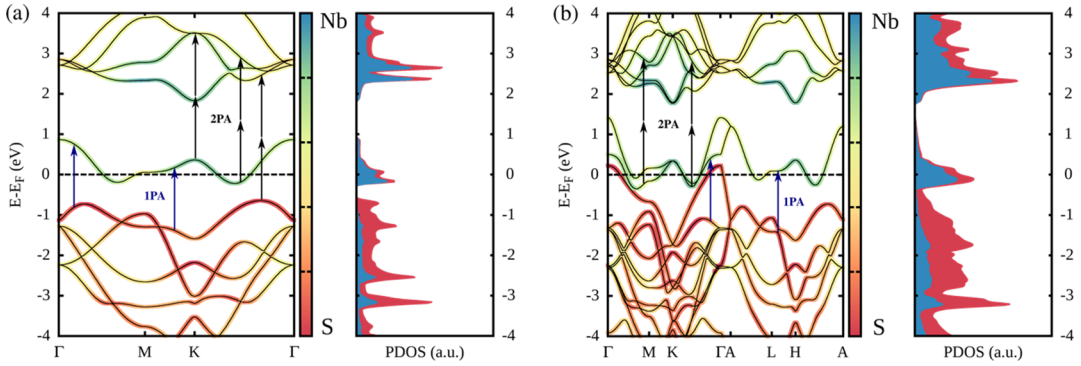

Figure 10. Electronic band structure and projected density of states (PDOS) of 2H–NbS_2: (a) monolayer; (b) bulk. Projections on the Nb orbitals are represented in blue while projections on the S orbitals are represented in red. One-photon absorption (1 PA) and two-photon absorption (2 PA) are depicted in blue and black, respectively.

https://dx.doi.org/10.1021/acs.jpcc.0c02383
J. Phys. Chem. C 2020, 124, 15425−15433

Manoel L. da Silva Neto − *Graduate Program in Materials Science, Universidade Federal de Pernambuco, 50670-901 Recife-PE, Brazil;* orcid.org/0000-0003-2597-287X
Pilar G. Vianna − *MackGraphe, Universidade Presbiteriana Mackenzie, 01302-907 São Paulo-SP, Brazil;* orcid.org/0000-0001-9767-5538
Henrique B. Ribeiro − *MackGraphe, Universidade Presbiteriana Mackenzie, 01302-907 São Paulo-SP, Brazil*
Vanessa O. Gordo − *MackGraphe, Universidade Presbiteriana Mackenzie, 01302-907 São Paulo-SP, Brazil*
Isabel C. S. Carvalho − *Department of Physics, PUC-Rio, 22451-900 Rio de Janeiro-RJ, Brazil*
Cid B. de Araújo − *Physics Department and Graduate Program in Materials Science, Universidade Federal de Pernambuco, 50670-901 Recife-PE, Brazil;* orcid.org/0000-0003-1205-9467
Christiano J. S. de Matos − *MackGraphe, Universidade Presbiteriana Mackenzie, 01302-907 São Paulo-SP, Brazil;* orcid.org/0000-0001-6165-3791
Leandro Seixas − *MackGraphe, Universidade Presbiteriana Mackenzie, 01302-907 São Paulo-SP, Brazil;* orcid.org/0000-0001-7420-0708
Ali M. Jawaid − *Materials and Manufacturing Directorate, Air Force Research Laboratories, Wright-Patterson AFB, Ohio 45433, United States*
Robert Busch − *Materials and Manufacturing Directorate, Air Force Research Laboratories, Wright-Patterson AFB, Ohio 45433, United States*
Allyson J. Ritter − *Materials and Manufacturing Directorate, Air Force Research Laboratories, Wright-Patterson AFB, Ohio 45433, United States*
Richard A. Vaia − *Materials and Manufacturing Directorate, Air Force Research Laboratories, Wright-Patterson AFB, Ohio 45433, United States;* orcid.org/0000-0003-4589-3423
Anderson S. L. Gomes − *Physics Department, Universidade Federal de Pernambuco, 50670-901 Recife-PE, Brazil*

Complete contact information is available at: https://pubs.acs.org/10.1021/acs.jpcc.0c02383

Author Contributions

#M.M. and M.L.d.S.N. contributed equally to this work.

Notes

The authors declare no competing financial interest.

■ ACKNOWLEDGMENTS

The authors thank financial support from CNPq, FACEPE, and CAPES. A.S.L.G., C.J.S.d.M., P.G.V., V.O.G., and M.M. acknowledge support from AFOSR. A.M.J., A.J.R., and R.A.V. thank AFOSR and the Air Force Research Laboratory Materials and Manufacturing Directorate for financial support. CJSdM acknowledges support from FAPESP (SPEC project no. 2012/50259-8 and Thematic Project no. 2015/11779-4), the Brazilian Nanocarbon Institute of Science and Technology (INCT/Nanocarbono), and CAPES−PRINT (Programa Institucional de Internacionalização; grant # 88887.310281/2018-00). L.S. acknowledges LoboC/NACAD/UFRJ for high-performance computing facilities. V.O.G. and P.G.V. acknowledge CAPES for a post-doctoral and a Ph.D. fellowship, respectively. H.B.R. acknowledges FAPESP for post-doctoral fellowships (grant numbers 2018/04926-9 and 2017/20100-00).

■ REFERENCES

(1) Wei, Z.; Li, B.; Xia, C.; Cui, Y.; He, J.; Xia, J.-B.; Li, J. Various structures of 2D transition-metal dichalcogenides and Their Applications. *Small Methods* **2018**, *2*, 1800094.
(2) Krasnok, A.; Lepeshov, S.; Alú, A. Nanophotonics with 2D transition metal dichalcogenides [Invited]. *Opt. Express* **2018**, *26*, 15972−15994.
(3) Choi, W.; Choudhary, N.; Han, G. H.; Park, J.; Akinwande, D.; Lee, Y. H. Recent development of two-dimensional transition metal dichalcogenides and their applications. *Mater. Today* **2017**, *20*, 116−130.
(4) Han, S. A.; Bhatia, R.; Kim, S. Synthesis, properties and potential applications of two-dimensional transition metal dichalcogenides. *Nano Convergence* **2015**, *2*, 17.
(5) Huo, N.; Yang, Y.; Li, J. Optoelectronics based on 2D TMDs and heterostructures. *J. Semicond.* **2017**, *38*, 031002.
(6) Kurapati, R.; Kostarelos, K.; Prato, M.; Bianco, A. Biomedical uses for 2D materials beyond graphene: current advances and challenges. *Adv. Mater.* **2016**, *28*, 6052−6074.
(7) Autere, A.; Jussila, H.; Dai, Y.; Wang, Y.; Lipsanen, H.; Sun, Z. Nonlinear optics with 2d layered materials. *Adv. Mater.* **2018**, *30*, 1705963.
(8) Kumar, N.; Najmaei, S.; Cui, Q.; Ceballos, F.; Ajayan, P. M.; Lou, J.; Zhao, H. Second harmonic microscopy of monolayer MoS_2. *Phys. Rev. B: Condens. Matter Mater. Phys.* **2013**, *87*, 161403.
(9) Janisch, C.; Mehta, N.; Ma, D.; Elías, A. L.; Perea-López, N.; Terrones, M.; Liu, Z. Ultrashort optical pulse characterization using WS_2 monolayers. *Opt. Lett.* **2014**, *39*, 383−385.
(10) Woodward, R. I.; Phelan, C. F.; Murray, R. T.; de Oliveira, R. E. P.; Runcorn, T. H.; Kelleher, E. J. R.; Li, S.; Oliveira, E. C. de.; Fechine, G. J. M.; Eda, G.; et al. Characterization of the second-and third-order nonlinear optical susceptibilities of monolayer MoS_2 using multiphoton microscopy. *2D Mater* **2017**, *4*, 011006.
(11) Cui, Q.; Muniz, R. A.; Sipe, J. E.; Zhao, H. Strong and anisotropic third-harmonic generation in monolayer and multilayer ReS_2. *Phys. Rev. B* **2017**, *95*, 165406.
(12) Säynätjoki, A.; Karvonen, L.; Rostami, H.; Autere, A.; Mehravar, S.; Lombardo, A.; Norwood, R.; Hasan, T.; Peyghambarian, N.; Lipsanen, H.; et al. Ultra-strong nonlinear optical processes and trigonal warping in MoS_2 layers. *Nat. Commun.* **2017**, *8*, 893.
(13) Li, D.; Xiong, W.; Jiang, L.; Xiao, Z.; Rabiee Golgir, H.; Wang, M.; Huang, X.; Zhou, Y.; Lin, Z.; Song, J.; et al. Multimodal nonlinear optical imaging of MoS_2 and MoS_2-based Van der Waals heterostructures. *ACS Nano* **2016**, *10*, 3766−3775.
(14) Ducharme, H.; Li, Y.; You, Y. S.; Ghimire, S.; Heinz, T. F.; Reis, D. A. High-harmonic generation from an atomically thin semiconductor. *Nature Phys* **2017**, *13*, 262−265.
(15) Wang, K.; Wang, J.; Fan, J.; Lotya, M.; O'Neill, A.; Fox, D.; Feng, Y.; Zhang, X.; Jiang, B.; Zhao, Q.; et al. Ultrafast saturable absorption of two-dimensional MoS_2 nanosheets. *ACS Nano* **2013**, *7*, 9260−9267.
(16) Zhang, N.; Li, Y.; Zhang, S.; McEvoy, N.; Gatensby, R.; Duesberg, G. S.; Wang, J. Saturation of two-photon absorption in layered transition metal dichalcogenides: experiment and theory. *ACS Photonics* **2018**, *5*, 1558−1565.
(17) Li, Y.; Dong, N.; Zhang, S.; Zhang, X.; Feng, Y.; Wang, K.; Zhang, L.; Wang, J. Giant two-photon absorption in monolayer MoS_2. *Laser Photon. Rev.* **2015**, *9*, 427−434.
(18) Dong, N.; Zhang, S.; Li, Y.; Wang, J. In *Organic Photonic Materials and Devices XX. Proceedings of SPIE OPTO, San Francisco—California, USA, 27 January, 01 February, 2018*; Tabor, E. C., Kajzar, F., Kaino, T., Koyke, Y., Eds.; SPIE San Francisco, 2018.
(19) Dong, N.; Li, Y.; Feng, Y.; Zhang, S.; Zhang, X.; Chang, C.; Fan, J.; Zhang, L.; Wang, J. Optical limiting and theoretical modelling of layered transition metal dichalcogenide nanosheets. *Sci. Rep.* **2015**, *5*, 14646.
(20) Varma, S. J.; Kumar, J.; Liu, Y.; Layne, K.; Wu, J.; Liang, C.; Nakanishi, Y.; Aliyan, A.; Yang, W.; Ajayan, P. M.; et al. 2D TiS_2

layers: a superior nonlinear optical limiting material. *Adv. Opt. Mater.* **2017**, *5*, 1700713.
(21) Thomas, K.; Feng, Y.; Chang, C.; Zhan, J.; Wang, C.; Zhao, Q.; Coleman, J. N.; Zhang, L.; Blau, W. J.; Wang, J. Broadband ultrafast nonlinear absorption and nonlinear refraction of layered molybdenum dichalcogenide semiconductors. *Nanoscale* **2014**, *6*, 10530−10535.
(22) Zheng, X.; Zhang, Y.; Chen, R.; Cheng, X. a.; Xu, Z.; Jiang, T. Z-scan measurement of the nonlinear refractive index of monolayer WS_2. *Opt. Express* **2015**, *23*, 15616−15623.
(23) Bikorimana, S.; Lama, P.; Walser, A.; Dorsinville, R.; Anghel, S.; Mitioglu, A.; Micu, A.; Kulyuk, L. Nonlinear optical responses in two-dimensional transition metal dichalcogenide multilayer: WS_2, WSe_2, MoS_2, and $Mo_{0.5}W_{0.5}S_2$. *Opt. Express* **2016**, *24*, 26998.
(24) Jawaid, A.; Che, J.; Drummy, L. F.; Bultman, J.; Waite, A.; Hsiao, M.-S.; Vaia, R. A. Redox exfoliation of layered transition metal dichalcogenides. *ACS Nano* **2017**, *11*, 635−646.
(25) Sheik-Bahae, M.; Said, A. A.; Wei, T.-H.; Hagan, D. J.; Van Stryland, E. W. Sensitive measurement of optical nonlinearities using a single beam. *IEEE J. Quantum Electron.* **1990**, *26*, 760−769.
(26) de Araújo, C. B.; Gomes, A. S. L.; Boudebs, G. Techniques for nonlinear optical characterization of materials: a review. *Rep. Prog. Phys.* **2016**, *79*, 036401.
(27) Backes, C.; Szydłowska, B. M.; Harvey, A.; Yuan, S.; Vega-Mayoral, V.; Davies, B. R.; Zhao, P.-l.; Hanlon, D.; Santos, E. J. G.; Katsnelson, M. I.; et al. Production of highly monolayer enriched dispersions of liquid exfoliated nanosheets by liquid cascade centrifugation. *ACS Nano* **2016**, *10*, 1589−1601.
(28) Blau, R.; Khalsa, G.; Schaefer, B. T.; Jarjour, A.; Rouvimov, S.; Nowack, K. C.; Xing, H. G.; Jena, D. Thickness dependence of superconductivity in ultrathin NbS_2. *Appl. Phys. Express* **2019**, *12*, 023008.
(29) McMullan, W. G.; Irwin, J. C. Raman scattering from 2H and 3R−NbS_2. *Solid State Commun.* **1983**, *45*, 557−560.
(30) Zhou, K.-G.; Zhao, M.; Chang, M.-J.; Wang, Q.; Wu, X.-Z.; Song, Y.; Zhang, H.-L. Size-dependent nonlinear optical properties of atomically thin transition metal dichalcogenide nanosheets. *Small* **2015**, *11*, 694−701.
(31) Zhao, S.; Hotta, T.; Koretsune, T.; Watanabe, K.; Taniguchi, T.; Sugawara, K.; Takahashi, T.; Shinohara, H.; Kitaura, R. Two-dimensional metallic NbS2 growth, optical identification and transport properties. *2D Mater.* **2016**, *3*, 025027.
(32) Iliopoulos, K.; Potamianos, D.; Kakkava, E.; Aloukos, P.; Orfanos, I.; Couris, S. Ultrafast third order nonlinearities of organic solvents. *Opt. Express* **2015**, *23*, 24171−24176.
(33) Hohenberg, P.; Kohn, W. Inhomogeneous electron gas. *Phys. Rev.* **1964**, *136*, 864B−871B.
(34) Kohn, W.; Sham, L. J. Self-consistent equations including exchange and correlation effects. *Phys. Rev.* **1965**, *140*, A1133−A1138.
(35) Soler, J. M.; Artacho, E.; Gale, J. D.; García, A.; Junquera, J.; Ordejón, P.; Sánchez-Portal, D. The SIESTA method for ab initio order-N materials simulation. *J. Phys.: Condens. Matter* **2002**, *14*, 2745−2779.
(36) Troullier, N.; Martins, J. L. Efficient pseudopotentials for planewave calculations. *Phys. Rev. B: Condens. Matter Mater. Phys.* **1991**, *43*, 1993−2006.
(37) Vydrov, O. A.; Van Voorhis, T. Nonlocal Van der Waals density functional: the simpler the better. *J. Chem. Phys.* **2010**, *133*, 244103.
(38) Monkhorst, H. J.; Pack, J. D. Special points for brillouin-zone integrations. *Phys. Rev. B: Solid State* **1976**, *13*, 5188.
(39) Olesiak-Banska, J.; Waszkielewicz, M.; Obstarczyk, P.; Samoc, M. Two-photon absorption and photoluminescence of colloidal gold nanoparticles and nanoclusters. *Chem. Soc. Rev.* **2019**, *48*, 4087−4117.
(40) de Oliveira, N. T. C.; Reyna, A. S.; Falcão, E. H. L.; de Araújo, C. B. Light scattering, absorption and refraction due to high-order optical nonlinearities in coloidal gold nanorods. *J. Phys. Chem. C* **2019**, *123*, 12997−13008.
(41) van Loon, E. G. C. P.; Rösner, M.; Schönhoff, G.; Katsnelson, M. I.; Wehling, T. O. Competing Coulomb and electron−phonon interactions in NbS_2. *npj Quantum Mater.* **2018**, *3*, 32.
(42) Li, L.; Pang, L.; Zhao, Q.; Wang, Y.; Liu, W. Niobium disulfide as a new saturable absorber for an ultrafast fibre laser. *Nanoscale* **2020**, *12*, 4537−4543.
(43) Reyna, A. S.; de Araújo, C. B. High-order optical nonlinearities in plasmonic nanocomposites — a review. *Adv. Opt. Photonics* **2017**, *9*, 720−774.

https://dx.doi.org/10.1021/acs.jpcc.0c02383
J. Phys. Chem. C 2020, 124, 15425−15433